JACC: CARDIOVASCULAR IMAGING, VOL. 2, NO. 6, 2009
JUNE 2009:720–8

Table 1. Baseline Clinical and Angiographic Characteristics

	HIP (n = 17)	Non-HIP (n = 7)	p Value
Age, yrs, mean ± SD	66 ± 9	66 ± 12	NS
Sex, male/female	14/3	4/3	NS
Diagnosis			
AP/UAP	14/3	5/2	NS
Number of CAD			
SVD/MVD	9/8	3/4	NS
Coronary risk factors, n (%)			
Hypertension	14 (82.4%)	3 (42.9%)	NS
Hypercholesterolemia	13 (76.5%)	4 (57.1%)	NS
Diabetes mellitus	7 (41.2%)	2 (28.6%)	NS
Current smoking	4 (23.5%)	3 (42.9%)	NS
Target vessel, n (%)			0.047
LAD	11 (61.1%)	4 (57.1%)	
LCX	0 (0%)	2 (28.6%)	
RCA	7 (38.9%)	1 (14.3%)	

AP = angina pectoris; CAD=coronary artery disease; HIP = hyperintense plaque; LAD = left descending artery; LCX = left circumflex artery; MVD = multivessel disease; NS = not significant; RCA = right coronary artery; SD = standard deviation; SVD = single vessel disease; UAP = unstable angina pectoris.

The frequency of spotty calcification tended to be higher in HIP lesions (89% vs. 50%, $p = 0.079$). Positive remodeling based on IVUS examinations was observed in 17 (94%) of the 18 patients with HIP, which is significantly higher than in non-HIP patients (14%, $p < 0.0001$). The frequency of ultrasound attenuation was significantly higher in HIP lesions (100% vs. 14%, $p < 0.0001$). The kappa statistics for interobserver agreement for ultrasound attenuation was 0.87 (substantial agreement). Transient coronary slow-flow phenomena were observed immediately after either first balloon dilation or stent implantation in 15 (83%) of the 18 patients with HIP, which is significantly higher than in non-HIP patients (14%, $p < 0.01$). Comparisons of CMR with both MSCT and IVUS of representative cases with HIP are shown in Figures 3 and 4.

DISCUSSION

This is the first report to systematically evaluate the components of HIP detected by noncontrast T1WI in CMR using both MSCT and IVUS examinations. Our findings demonstrate that typical coronary HIP is associated with a high frequency of ultrasound attenuation and positive remodeling, remarkably low CT density, and a high incidence of transient slow-flow phenomena. These results indicate that noncontrast T1WI in CMR is a useful technique for characterization of coronary plaque components.

Coronary plaque imaging with noncontrast T1WI was first reported by Maintz et al. (19) and Yeon et al. (8). These investigators speculated that a hyperintense signal in coronary plaques on noncontrast T1WI indicates the presence of mural or intraplaque thrombus containing methemoglobin. However, these investigators did not systematically evaluate the properties of hyperintense signals in coronary plaques. In our study, the properties of the HIP on noncontrast T1W CMR were examined by using both MSCT and IVUS imaging obtained before PCI. We used noncontrast T1W inversion-recovery and fat-suppressed 3-dimensional black-blood gradient-echo sequence on a 1.5-T MR system. This technique has successfully yielded a description of HIP similar to those observed in the carotid artery (9,20). Recently, our group showed that by using this technique HIP could be observed in the area corresponding to the low-density coronary plaques with positive coronary remodeling observed by MSCT.

Comparison between CMR images and MSCT and IVUS. Using MSCT, HIP has a significantly higher frequency of positive remodeling and lower CT density in comparison with non-HIP. The frequency of spotty calcification tended to be higher in HIP. Noncalcified plaques <30 HU on MSCT correlated with the presence of a lipid-rich necrotic core (21); the presence of 3 features of coronary plaque on MSCT (positive remodeling, noncalcified plaque <30 HU, and spotty calcification) provided a high level of confidence for the characterization of vulnerable plaques associated with acute coronary syndrome (14). In the present study, all 18 HIP cases displayed significantly lower CT values, and 80% of them presented on MSCT with the aforementioned 3 typical features; in contrast, none of the non-HIP cases exhibited those 3 features. These findings suggest that observation of HIP on noncontrast T1WI may reflect the potential for plaque vulnerability.

In comparisons with IVUS images, HIP also has a significantly higher frequency of positive remodeling and ultrasound attenuation than non-HIP. In this study, positive coronary remodeling was observed with a higher frequency in HIP on both MSCT and IVUS. Positive remodeling associated with a plaque is thought to reflect a compensatory enlargement to avoid the decrease of the coronary lumen (22). On the other hand, Varnava et al. (23) performed a pathological

Table 2. Lesion Characteristics and Clinical Results of HIP/Non-HIP on CMR, MSCT, and IVUS

				MSCT				IVUS			
Lesion	Target		PMR	PR	RI	Minimum CT Density (HU)	Spotty Calcification	UA*	PR	RI	Slow Flow
HIP											
1	LAD	Seg 6	3.93	Yes	1.30	−50	Yes	++	Yes	1.18	Yes
2	LAD	Seg 6	2.63	Yes	1.27	−32	No	++	Yes	1.29	Yes
3	LAD	Seg 6	2.09	Yes	1.18	−19	Yes	++	Yes	1.15	Yes
4	RCA	Seg 3	2.03	Yes	1.17	−66	Yes	+	Yes	1.13	Yes
5	LAD	Seg 6	1.98	No	1.03	−26	Yes	+	Yes	1.14	No
6	RCA	Seg 1	1.78	Yes	1.27	−19	Yes	++	Yes	1.11	No
7	RCA	Seg 3	1.78	Yes	1.15	−7	Yes	++	Yes	1.13	Yes
8	RCA	Seg 3	1.76	Yes	1.24	−44	Yes	+	Yes	1.11	Yes
9	LAD	Seg 6	1.67	Yes	1.24	−3	No	+	Yes	1.15	Yes
10	RCA	Seg 3	1.56	Yes	1.27	−12	Yes	+	Yes	1.26	Yes
11	LAD	Seg 7	1.45	Yes	1.12	−42	Yes	+	Yes	1.08	Yes
12	RCA	Seg 2	1.27	Yes	1.20	−16	Yes	++	Yes	1.19	Yes
13	RCA	Seg 1	1.24	Yes	1.10	−18	Yes	++	Yes	1.16	Yes
14	LAD	Seg 7	1.14	No	1.04	0	Yes	+	No	1.02	Yes
15	LAD	Seg 6	1.12	Yes	1.27	−41	Yes	+	Yes	1.21	Yes
16	LAD	Seg 6	1.05	Yes	1.13	−37	Yes	++	Yes	1.09	No
17	LAD	Seg 6	1.05	Yes	1.26	2	Yes	+	Yes	1.17	Yes
18	LAD	Seg 6	1.01	Yes	1.19	12	Yes	++	Yes	1.08	Yes
Non-HIP											
1	LAD	Seg 6	0.98	No	1.07	−21	No†	+	Yes	1.09	Yes
2	RCA	Seg 2	0.97	No	0.96	28	Yes	−	No	0.85	No
3	LAD	Seg 7	0.94	No	0.97	8	No	−	No	0.93	No
4	LAD	Seg 7	0.94	No	0.99	12	Yes	−	No	0.82	No
5	LCX	Seg11	0.89	No	0.99	37	Yes	−	No	0.95	No
6	LAD	Seg 6	0.86	No	0.97	15	No	−	No	0.88	No
7	LCX	Seg 15	0.74	No	0.92	−12	No	−	No	0.73	No

*Ultrasound attenuation category: − = no ultrasound attenuation, + = arc of attenuation <180°, ++ = arc of attenuation ≥180°. †Large calcification was observed.
CMR = cardiac magnetic resonance; CT = computed tomography; HU = Hounsfield unit; IVUS = intravascular ultrasound; MSCT = multislice computed tomography; PMR = intensity of coronary plaque to cardiac muscle ratio; PR = positive remodeling; RI = remodeling index; Seg = segment; UA = ultrasound attenuation; other abbreviations as in Table 1.

examination of positive remodeling plaques and reported that they have higher lipid content and macrophage count; these 2 findings are recognized pathological markers for plaque vulnerability. Furthermore, positive remodeling plaques have a larger fibro-fatty component according to the IVUS radiofrequency data (24,25); these positive remodeling plaques are observed frequently in patients with acute coronary syndrome (14–16). Therefore, positive coronary remodeling is thought to have a potential for plaque vulnerability. In this study, the rate of positive remodeling was very high. However, in previous studies, the rate of positive remodeling of lesions subjected to elective PCI has not been very high (15,26,27). This discrepancy may relate to the characteristics of HIP. As we have already mentioned, HIP is strongly associated with a remarkably low CT density and a high frequency of

Table 3. Characteristics in Hyperintense and Normointense Plaque

	HIP (n = 18)	Non-HIP (n = 7)	p Value
PMR	1.70 ± 0.71	0.90 ± 0.08	0.0081
MSCT			
Positive remodeling, yes/no	16/2	0/7	<0.0001
RI	1.19 ± 0.08	0.98 ± 0.05	<0.0001
Minimal CT density, HU	−23.2 ± 20.7	9.6 ± 20.5	0.0016
Spotty calcification, yes/no	16/2	3/3*	0.079
IVUS			
Positive remodeling, yes/no	17/1	1/6	<0.001
RI	1.15 ± 0.07	0.89 ± 0.11	<0.0001
Ultrasound attenuation, yes/no	18/0	1/6	<0.0001
Slow flow phenomenon, yes/no	15/3	1/6	0.003

*One excluded because of large calcification.
Abbreviations as in Tables 1 and 2.

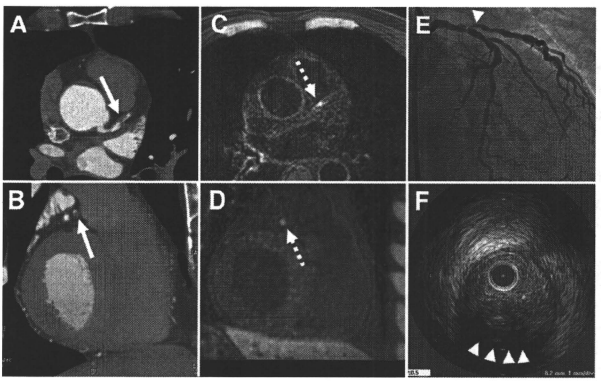

Figure 3. Representative Case of HIP in the Proximal LAD

A 60-year-old patient with a severe coronary stenosis in the proximal left descending artery (LAD) is shown. Multislice computed tomography (MSCT) (**A:** horizontal, **B:** sagittal) demonstrates the low-density positive remodeling plaque (–32 Hounsfield units, remodeling index: 1.27) **(arrow)** with severe coronary stenosis in the proximal LAD. On the corresponding cardiac magnetic resonance (CMR) (**C:** horizontal, **D:** sagittal), this low-density plaque was visualized as a "hyperintense spot" **(dashed arrow)**. On the coronary angiography, severe coronary stenosis was observed **(E) (arrowhead)**, and on IVUS examination **(F)**, positive remodeling plaque (remodeling index: 1.29) with ultrasound attenuation **(arrowheads)** was observed in the proximal LAD, corresponding with the plaque observed by both MSCT and CMR. HIP = hyperintense plaque; IVUS = intravascular ultrasound.

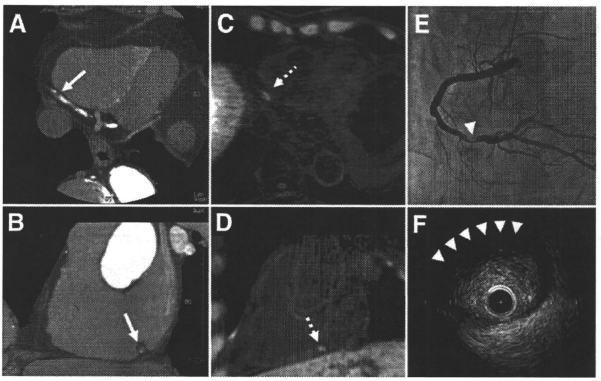

Figure 4. Representative Case of HIP in the Mid-RCA

A 60-year-old patient with a severe coronary stenosis in the mid-right coronary artery (RCA) is shown. Multislice computed tomography (MSCT) (**A:** horizontal, **B:** sagittal) shows the low-density positive remodeling plaque (–66 Hounsfield units, remodeling index: 1.15, **arrow**) with severe coronary stenosis in the mid-RCA. On the corresponding cardiac magnetic resonance (CMR) (**C:** horizontal, **D:** sagittal), a hyperintense plaque (HIP) can be observed by MSCT in the region with a low-density positive remodeling plaque **(dashed arrow)**. On the coronary angiography, severe coronary stenosis was observed **(E)**. On intravascular ultrasound examination **(F)**, positive remodeling plaque (remodeling index: 1.13) with ultrasound attenuation **(white arrowheads)** was observed in the mid-RCA, corresponding with the plaque observed both by MSCT and CMR.

positive remodeling. These factors are recognized surrogate markers for vulnerable coronary plaques (14). Thus, the present findings—that in stable angina patients with HIP the rate of positive remodeling was high and similar to those for cases of acute coronary syndrome (15)—may be explained by the possibility that HIP may represent vulnerable coronary plaque. In other words, HIP itself may reflect positive remodeling, which represents a large volume of lipid content.

The mechanism of ultrasound attenuation is thought to involve the existence of microcalcification, thrombus, cholesterol crystals with expansive positive arterial remodeling (20,28), and large lipid-rich necrotic core (29,30). Furthermore, in histological IVUS examination, the necrotic core is significantly larger in plaques with ultrasound attenuation (20). On the other hand, it is well known that slow-flow/no-reflow phenomena may occur with high frequency during PCI treatment of ultrasound-attenuated plaques (18,28,29,31). In our study, transient slow-flow phenomena occurred in 15 (83%) of the 18 lesions with ultrasound attenuation in HIP, in contrast, only 1 (14%) of the 7 lesions without ultrasound attenuation in non-HIP behaved this way. Thus, HIP is thought to represent a great potential for high-risk plaque, which induces transient slow-flow phenomena during PCI.

Clinical impact of HIP on noncontrast T1W CMR. In the studies of the carotid artery using magnetic resonance imaging, HIP on T1WI has been reported with a histological correlation with methemoglobin in intraplaque hemorrhage (9,10). Because intraplaque hemorrhage is a criterion for complicated plaque (American Heart Association type VI) and patients with this type of carotid plaque exhibited ischemic cerebrovascular events and were therefore recognized as cases of vulnerable carotid plaque (10,11), noncontrast T1WI in CMR may enable noninvasive detection of advanced coronary plaque stages, such as carotid plaque. Based on carotid artery studies and our findings from MSCT and IVUS in this study, we speculate that the observed high signals in coronary plaque generated by noncontrast T1WI may represent intraplaque hemorrhage or lipid-rich necrotic cores and, therefore, may have potential as markers for plaque vulnerability.

Although the characterization of atherosclerotic plaque with a noninvasive imaging modality is still challenging, our findings detected by noncontrast T1WI may be informative findings to identify the plaque characteristics. Noninvasive, easily repeatable, and inexpensive methods that detect instability of coronary lesions are needed for the management of patients with high-risk coronary artery disease. In this regard, coronary plaque imaging using noncontrast T1WI may provide clinically important information regarding plaque vulnerability and clinical outcome. Further prospective studies are warranted to elucidate whether HIP has potential as a marker for vulnerability and clinical outcomes.

Study limitations. The number of subjects in this study was small. In addition, recruiting patients with significant coronary stenosis might have resulted in a certain bias, because IVUS examination is an invasive technique with associated non-negligible risks, and it is permitted only during PCI. Therefore, patients without significant coronary stenosis were excluded. However, IVUS is the current in vivo gold standard for coronary plaque assessment and is the only way to differentiate plaque characterization. Thus, we have chosen a group of selected patients with significant coronary stenosis. Because no comparison with histopathological data was performed in this study, precise characterization of HIP remains unknown. From the knowledge of carotid plaque evaluation using magnetic resonance imaging and pathological examination, the observed high signals generated by short T_1 plaques may represent intraplaque hemorrhage or necrotic lipid cores. These assumptions remain to be investigated in subsequent studies, and histological correlation is required for verification. Furthermore, only T1WI was used in this study. The time-of-flight image was considered to be a useful method for distinguishing intraplaque hemorrhage from lipid-rich necrotic cores (30). Another limitation of this study is that study patients presented with stable angina pectoris but not acute coronary syndrome; therefore, it remains unknown whether HIP detected by T1WI represents really vulnerable coronary plaques.

CONCLUSIONS

Hyperintense plaque on noncontrast T1WI is strongly associated with positive coronary remodeling, remarkably low CT density, and ultrasound attenuation. Thus, the data suggest that HIP detected by noncontrast T1WI may have potential for identifying vulnerable coronary lesions.

Reprint requests and correspondence: Dr. Tomohiro Kawasaki, Cardiovascular Center, Shin-Koga Hospital, 120, Tenjin-cho, Kurume 830-8577, Japan. *E-mail: tokawasaki@mug.biglobe.ne.jp.*

REFERENCES

1. Botnar RM, Stuber M, Kissinger KV, Kim WY, Spuentrup E, Manning WJ. Noninvasive coronary vessel wall and plaque imaging with magnetic resonance imaging. Circulation 2000; 102:2582–7.
2. Kim WY, Astrup AS, Stuber M, et al. Subclinical coronary and aortic atherosclerosis detected by magnetic resonance imaging in type 1 diabetes with and without diabetic nephropathy. Circulation 2007;115:228–35.
3. Kim WY, Stuber M, Bornert P, Kissinger KV, Manning WJ, Botnar RM. Three-dimensional black-blood cardiac magnetic resonance coronary vessel wall imaging detects positive arterial remodeling in patients with nonsignificant coronary artery disease. Circulation 2002;106:296–9.
4. Ferencik M, Nieman K, Achenbach S. Noncalcified and calcified coronary plaque detection by contrast-enhanced multi-detector computed tomography: a study of interobserver agreement. J Am Coll Cardiol 2006;47: 207–9.
5. Kopp AF, Schroeder S, Baumbach A, et al. Non-invasive characterisation of coronary lesion morphology and composition by multislice CT: first results in comparison with intracoronary ultrasound. Eur Radiol 2001;11:1607–11.
6. Ropers D, Baum U, Pohle K, et al. Detection of coronary artery stenoses with thin-slice multi-detector row spiral computed tomography and multiplanar reconstruction. Circulation 2003;107:664–6.
7. Schroeder S, Kopp AF, Baumbach A, et al. Noninvasive detection and evaluation of atherosclerotic coronary plaques with multislice computed tomography. J Am Coll Cardiol 2001; 37:1430–5.
8. Yeon SB, Sabir A, Clouse M, et al. Delayed-enhancement cardiovascular magnetic resonance coronary artery wall imaging: comparison with multislice computed tomography and quantitative coronary angiography. J Am Coll Cardiol 2007;50:441–7.
9. Moody AR, Murphy RE, Morgan PS, et al. Characterization of complicated carotid plaque with magnetic resonance direct thrombus imaging in patients with cerebral ischemia. Circulation 2003;107:3047–52.
10. Murphy RE, Moody AR, Morgan PS, et al. Prevalence of complicated carotid atheroma as detected by magnetic resonance direct thrombus imaging in patients with suspected carotid artery stenosis and previous acute cerebral ischemia. Circulation 2003;107: 3053–8.
11. Yamada N, Higashi M, Otsubo R, et al. Association between signal hyperintensity on T1-weighted MR imaging of carotid plaques and ipsilateral ischemic events. Am J Neuroradiol 2007;28:287–92.
12. Imazeki T, Sato Y, Inoue F, et al. Evaluation of coronary artery remodeling in patients with acute coronary syndrome and stable angina by multislice computed tomography. Circ J 2004;68:1045–50.
13. Ehara S, Kobayashi Y, Yoshiyama M, et al. Spotty calcification typifies the culprit plaque in patients with acute myocardial infarction: an intravascular ultrasound study. Circulation 2004; 110:3424–9.
14. Motoyama S, Kondo T, Sarai M, et al. Multislice computed tomographic characteristics of coronary lesions in acute coronary syndromes. J Am Coll Cardiol 2007;50:319–26.
15. Nakamura M, Nishikawa H, Mukai S, et al. Impact of coronary artery remodeling on clinical presentation of coronary artery disease: an intravascular ultrasound study. J Am Coll Cardiol 2001;37:63–9.
16. Schoenhagen P, Ziada KM, Kapadia SR, Crowe TD, Nissen SE, Tuzcu EM. Extent and direction of arterial remodeling in stable versus unstable coronary syndromes: an intravascular ultrasound study. Circulation 2000; 101:598–603.
17. Pasterkamp G, Borst C, Gussenhoven EJ, et al. Remodeling of de novo atherosclerotic lesions in femoral arteries: impact on mechanism of balloon angioplasty. J Am Coll Cardiol 1995;26:422–8.
18. Okura H, Taguchi H, Kubo T, et al. Atherosclerotic plaque with ultrasonic attenuation affects coronary reflow and infarct size in patients with acute coronary syndrome: an intravascular ultrasound study. Circ J 2007;71:648–53.
19. Maintz D, Ozgun M, Hoffmeier A, et al. Selective coronary artery plaque visualization and differentiation by contrast-enhanced inversion prepared MRI. Eur Heart J 2006;27:1732–6.
20. Yamada R, Okura H, Kume T, et al. Histological characteristics of plaque with ultrasonic attenuation: a comparison between intravascular ultrasound and histology. J Cardiol 2007;50: 223–8.
21. Motoyama S, Kondo T, Anno H, et al. Atherosclerotic plaque characterization by 0.5-mm-slice multislice computed tomographic imaging. Circ J 2007;71:363–6.
22. Glagov S, Weisenberg E, Zarins CK, Stankunavicius R, Kolettis GJ. Compensatory enlargement of human atherosclerotic coronary arteries. N Engl J Med 1987;316:1371–5.
23. Varnava AM, Mills PG, Davies MJ. Relationship between coronary artery remodeling and plaque vulnerability. Circulation 2002;105:939–43.
24. Fujii K, Carlier SG, Mintz GS, et al. Association of plaque characterization by intravascular ultrasound virtual histology and arterial remodeling. Am J Cardiol 2005;96:1476–83.
25. Higashikuni Y, Tanabe K, Yamamoto H, et al. Relationship between coronary artery remodeling and plaque composition in culprit lesions: an intravascular ultrasound radiofrequency analysis. Circ J 2007;71:654–60.
26. Okura H, Hayase M, Shimodozono S, Bonneau HN, Yock PG, Fitzgerald PJ. Impact of pre-interventional arterial remodeling on subsequent vessel behavior after balloon angioplasty: a serial intravascular ultrasound study. J Am Coll Cardiol 2001;38:2001–5.
27. Weissman NJ, Sheris SJ, Chari R, et al. Intravascular ultrasonic analysis of plaque characteristics associated with coronary artery remodeling. Am J Cardiol 1999;84:37–40.
28. Hara H, Tsunoda T, Moroi M, et al. Ultrasound attenuation behind coronary atheroma without calcification: mechanism revealed by autopsy. Acute Card Care 2006;8:110–2.
29. Furuichi S, Itoh A, Ishibashi-Ueda H, et al. Ultrasound attenuated coronary plaque as a risk factor for slow flow or no-reflow during percutaneous coronary intervention: a case report. J Cardiol 2007;49:193–7.
30. Yuan C, Mitsumori LM, Ferguson MS, et al. In vivo accuracy of multispectral magnetic resonance imaging for identifying lipid-rich necrotic cores and intraplaque hemorrhage in advanced human carotid plaques. Circulation 2001;104:2051–6.
31. Tanaka A, Kawarabayashi T, Nishibori Y, et al. No-reflow phenomenon and lesion morphology in patients with acute myocardial infarction. Circulation 2002;105:2148–52.

Key Words: coronary plaque imaging ■ cardiac magnetic resonance ■ multislice computed tomography ■ intravascular ultrasound.

Eur Radiol (2009) 19: 2060–2065
DOI 10.1007/s00330-009-1358-x

NEURO

Kensuke Uotani
Yoshiyuki Watanabe
Masahiro Higashi
Tetsuro Nakazawa
Atsushi K. Kono
Yoshiro Hori
Tetsuya Fukuda
Suzu Kanzaki
Naoaki Yamada
Toshihide Itoh
Kazuro Sugimura
Hiroaki Naito

Dual-energy CT head bone and hard plaque removal for quantification of calcified carotid stenosis: utility and comparison with digital subtraction angiography

Received: 27 August 2008
Revised: 24 November 2008
Accepted: 7 January 2009
Published online: 11 March 2009

K. Uotani · Y. Watanabe · M. Higashi · T. Nakazawa · A. K. Kono · Y. Hori · T. Fukuda · S. Kanzaki · N. Yamada · H. Naito
Department of Radiology,
National Cardiovascular Center,
Suita, Osaka, Japan

K. Uotani · K. Sugimura
Department of Radiology,
Kobe University Graduate
School of Medicine,
Kobe, Hyogo, Japan

T. Itoh
Siemens Asahi Medical Technologies,
Tokyo, Japan

K. Uotani (✉)
7-5-2 Kusuhoki-cho, Chuo-ku, Kobe,
Hyogo, 650-0017, Japan
e-mail: uota2@med.kobe-u.ac.jp
Tel.: +81-78-382-6104
Fax: +81-78-382-6129

Abstract We evaluated quantification of calcified carotid stenosis by dual-energy (DE) CTA and dual-energy head bone and hard plaque removal (DE hard plaque removal) and compared the results to those of digital subtraction angiography (DSA). Eighteen vessels (13 patients) with densely calcified carotid stenosis were examined by dual-source CT in the dual-energy mode (tube voltages 140 kV and 80 kV). Head bone and hard plaques were removed from the dual-energy images by using commercial software. Carotid stenosis was quantified according to NASCET criteria on MIP images and DSA images at the same plane. Correlation between DE CTA and DSA was determined by cross tabulation. Accuracies for stenosis detection and grading were calculated. Stenosis could be evaluated in all vessels by DE CTA after applying DE hard plaque removal. In contrast, conventional CTA failed to show stenosis in 13 out of 18 vessels due to overlapping hard plaque. Good correlation between DE plaque removal images and DSA images was observed (r^2=0.9504) for stenosis grading. Sensitivity and specificity to detect hemodynamically relevant (>70%) stenosis was 100% and 92%, respectively. Dual-energy head bone and hard plaque removal is a promising tool for the evaluation of densely calcified carotid stenosis.

Keywords Dual-source CT · Carotid stenosis · Dual-energy CT · Carotid plaque · CTA

Introduction

Recent clinical trials have proven that the degree of the internal carotid artery stenosis is associated with cerebral stroke. According to the North American Symptomatic Carotid Endarterectomy Trial (NASCET) and the European Carotid Surgery Trial, symptomatic patients with severe stenoses (70–99%) can therefore benefit from carotid endarterectomy [1–3].

Conventional digital subtraction angiography (DSA) has been the "gold standard" for the evaluation of the degree of carotid artery stenosis, but conventional DSA has a tendency to underestimate the degree of carotid artery stenosis because it uses a limited number of projections and can therefore fail to detect the maximum internal carotid artery stenosis. 3D evaluation of carotid stenosis has become possible with rotation angiography, but this method remains invasive and is still associated with catheter-related complications.

Recently, noninvasive MR angiography (MRA) and CT angiography (CTA) have partially replaced conventional angiography [4–9] in particular since CTA correlates well

with catheter angiography and has high diagnostic accuracy for 70–99% stenosis. Moreover, high-quality DSA-like images can be generated with 3D CTA and maximum intensity projection (MIP) technique to gain an overview of the target vessel, which can help to detect maximum carotid stenosis. Nevertheless, CTA still shows a lower sensitivity for quantifying stenosis in the presence of dense calcification or indwelling stents since these may obscure contrast material in the lumen [10].

With dual-energy dual-source CT, two images can be simultaneously acquired with different tube voltages, corresponding to different X-ray energies. Materials can then be differentiated by analyzing their attenuation differences depending on tube voltage. The attenuation difference between two X-ray energies is especially large in materials with high atomic numbers such as iodine due to the photo effect, thus bones and calcified plaques, which show a smaller attenuation difference, can be distinguished from iodine [11, 12]. As a result, calcified plaque (hard plaque) can be removed from vessels with iodine contrast together with bone removal and quantification of carotid stenosis even in the presence of dense calcifications may become possible.

Here, we compared dual-energy head bone and hard plaque removal (DE hard plaque removal), applied to dual-energy CTA images, with conventional digital subtraction angiography (DSA) with a focus on quantification of calcified carotid artery stenosis.

Materials and methods

This study was performed after approval of the local institutional review board. Written informed consent was obtained from all patients. In the period between June 2007 and December 2007, 16 patients with internal carotid artery stenosis underwent both carotid DSA and carotid CTA by using dual-source CT with dual-energy mode. Calcium volume was calculated on precontrast images by using a workstation (Zio M900 Quadra, Ziosoft, Japan). Patients with noncalcified or slightly calcified carotid stenosis (calcium volume$\leq$50 mm^3) were excluded. Finally, 13 patients with densely calcified carotid stenosis (calcium volume>50 mm^3) were enrolled and a total of 18 vessels were analyzed. CT angiography was performed using a dual-source multidetector CT system (SOMATOM Definition, Siemens, Germany). The dual-energy mode was operated with the following CT parameters: tube voltages of 140 kV and 80 kV, tube current–time products of 90 effective mA s and 380 effective mA s, respectively, a rotation time of 0.5 s per rotation, 64×0.6-mm collimation with z-flying focal spot and a pitch of 0.6. The contrast bolus was chosen according to the patients' body weight as 1 ml/kg of contrast material (350 mg I/ml) and injected for 20 s via the antecubital vein followed by 25 ml of saline. The delay before CT acquisition after injection was determined using bolus tracking software with a region of interest (ROI) was placed in a common carotid artery and a trigger threshold of 100 HU above the baseline. Two image datasets of different kV were reconstructed with 0.6-mm slice thickness and 0.6-mm slice gap. The reconstructed field of view was 200 mm. A soft convolution kernel (D30 kernel) was applied to obtain smooth 3D images. Dual-energy images of the carotids without bone and hard plaques were obtained from both datasets scanned at different tube voltage (Figs. 1 and 2) by using commercial postprocessing software (syngo 2008G, Siemens, Germany). We used the postprocessing software's default settings to remove cranial bone (head-bone removal). The combined images of both energy datasets were used for diagnostic reading and for 3D image (conventional CTA).

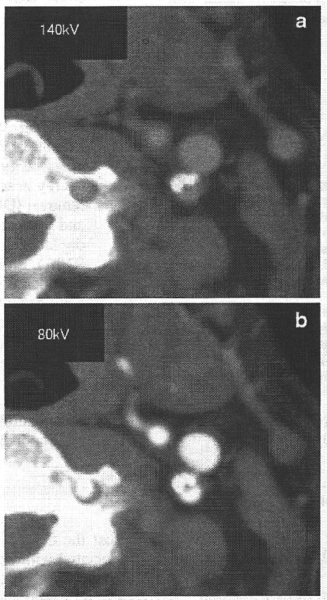

Fig. 1 Two images acquired by DSCT in the dual-energy mode at different tube voltages (140 kV and 80 kV) displayed with the same window width and window center (WW=600, WL=200). The densities of iodine and calcifications are higher in the 80-kV than in the 140-kV images, but the density difference of iodine between the 80-kV and 140-kV images is higher than that of calcifications

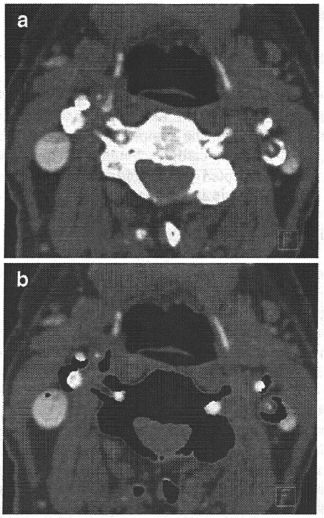

Fig. 2 **a** Combined image generated from two datasets obtained at different tube voltage. **b** Dual-energy CT image of a carotid artery eliminated hard plaques with application of DE hard plaque removal. The pixels detected as bone or calcifications are displayed with a CT number of −1,000 HU on the DE hard plaque removal CT image

DSA examinations were performed using a biplane DSA unit with rotational 3D DSA (INTEGRIS BV3000, Philips Healthcare, Best, Netherlands). Common carotid arteries were selectively catheterized, and anteroposterior, lateral, right anterior oblique, and left anterior oblique images were obtained.

Carotid artery stenosis was quantified according to NASCET criteria [1] on MIP images and on DSA images at the same plane. Carotid artery stenosis was measured independently by two experienced radiologists with 8 and 16 years of experience in vascular imaging. The readers evaluated the grade of stenosis according to the following scale: 0–25%, 25–50%, 50–75%, 75–99%. Interobserver variability was assessed using Cohen's kappa test. Correlation between CTA and DSA was determined by means of cross tabulation, and accuracy for detection and grading of stenosis was calculated.

Results

Evaluation of stenosis was possible for all vessels postprocessed with DE head bone and hard plaque removal software (Fig. 3). In contrast, conventional CTA did not allow the evaluation of stenosis in 13 out of 18 vessels on MIP images because calcifications covered the lumen. Good correlation (r^2=0.9504) was observed between the degree of carotid stenosis measured on CTA images after DE hard plaque removal and on DSA images (Fig. 4). Sensitivity and specificity for detecting hemodynamically relevant (>70%) stenosis was 100% and 92%, respectively.

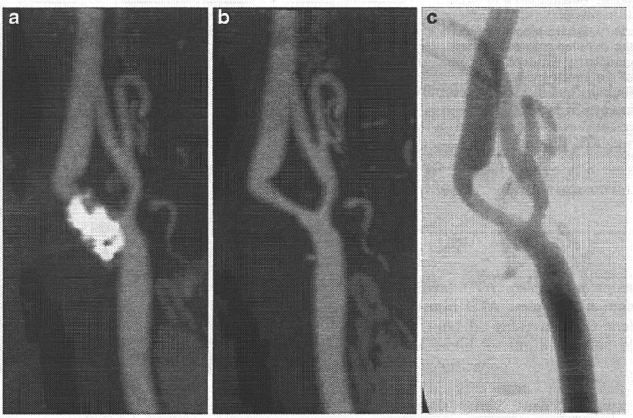

Fig. 3 **a** Conventional CTA image does not allow the visualization of the intravascular lumen due to the dense calcification. **b** CTA image after DE hard plaque removal: the calcification is almost completely removed and a quantification of stenosis is possible. The image quality is comparable with that of DSA (**c**)

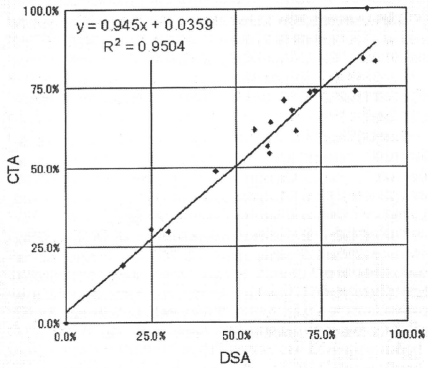

Fig. 4 Correlation between DE hard plaque removal CTA and DSA for the stenosis measurements. Good correlation between the two methods is observed (r^2=0.9504) for the quantification of carotid stenosis

One vessel with severe stenosis (87.4% according to DSA) was overestimated and displayed as a 99% stenosis-like lesion on the DE hard plaque removal CTA images (Fig. 5). Cohen's kappa test revealed a high level of interobserver agreement, with kappa coefficient being 0.91 for CTA and 0.73 for DSA, respectively (Table 1).

Discussion

Symptomatic patients with high grade carotid stenosis will benefit from carotid endarterectomy or stenting as secondary prevention of ischemic stroke [1–3]. The indication of these therapies is decided according to the degree of stenosis in addition to the symptoms experienced by the patient, thus precise carotid stenosis quantification is essential. The accepted gold standard for evaluation of carotid artery stenosis is catheter angiography; however, many reports have suggested that the sensitivity of multislice CTA (MSCTA) in evaluating the degree of carotid artery stenosis has become comparable with that of angiography while being associated with a lower level of risk [4–9].

Bone-subtraction CTA (BSCTA), where a nonenhanced scan is used to create a bone mask which is then subtracted from the contrast-enhanced CTA data, has been proven to be a robust method for the evaluation of intracranial vessels [13–15]. In this method, two volume datasets are matched for subtraction but, regarding neck bone and carotid artery calcification, misregistration errors are inevitable because neck bone and carotid arteries often move during pre- and postcontrast scan due to pulsation or neck movement [15]. In addition, the neck is more difficult to immobilize than the skull.

Our study showed that calcified plaques were almost completely removed from the carotids after applying DE bone removal and hard plaque removal postprocessing to dual-energy CTA images, and high quality DSA-like imaging was achieved. The results were in good correlation

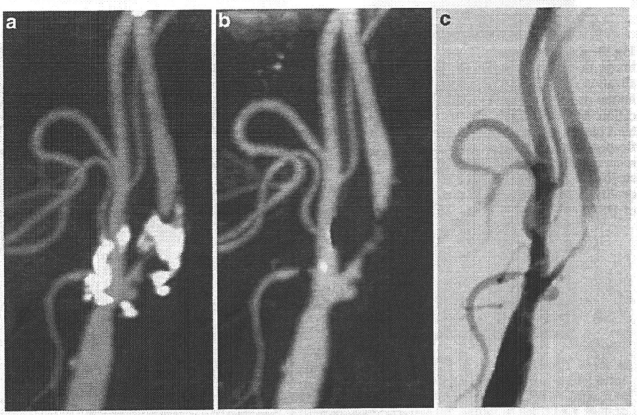

Fig. 5 **a** Conventional CTA image: quantification of stenosis is impossible. **b** CTA image after DE hard plaque removal: the calcified plaque is almost completely removed, yet parts of the lumen are as well, resulting in a display of a 99% stenosis-like lesion. **c** DSA image shows a patent lumen with 87% stenosis

Table 1 Interobserver agreement for assessment of stenosis on DE hard plaque removal CTA and DSA

CTA	0–25%	25–50%	50–75%	75–100%	Reader 2
0–25%	2				2
25–50%		3			3
50–75%			9	1	10
75–100%				3	3
Reader 1	2	3	9	4	
Kappa coefficient=0.91					

DSA	0–25%	25–50%	50–75%	75–100%	Reader 2
0–25%	1	1			2
25–50%		1	1		2
50–75%			9	1	10
75–100%				4	4
Reader 1	1	2	10	5	
Kappa coefficient=0.73					

with DSA in terms of quantification of carotid artery stenosis with dense calcifications. Although axial source image is reliable in grading stenosis, MIP reconstructions can be helpful when horizontal or tortuous course of the vessel or a very short stenosis can render the assessment of the stenosis difficult on axial images [16]. We used MIP images as the first-line method to quantify the degree of carotid stenosis because this study focused on feasibility of DE hard plaque removal. In clinical settings, axial source images were used in grading the degree of carotid artery stenosis in the presence of dense calcification.

Iodine shows a much larger increase in CT value with decreasing X-ray tube voltage than bone and calcification, which is the basis for iodine–bone separation using dual-energy CT. The voxels detected as bone or calcifications were displayed with a CT number of −1,000 HU on the DE hard plaque removal CTA images [11]. We found that the areas where bone or calcifications had been removed were slightly larger than the calcified plaques observed in the original images, meaning that calcifications seemed to be overestimated. This may be due to blooming artifacts or partial volume effects. Although moderate or mild stenosis measurements may be accurate, severe stenosis can be overestimated when the stenotic part runs very close to calcified plaque as was observed in one of our cases. This result can be altered by applying different kernels. Application of a hard kernel might clarify the border between calcification and iodine; however, we applied a relatively soft kernel (D30) to obtain smooth 3D images. According to theoretical considerations, image pixels with a CT value greater than 100 HU in the 140-kV image would be classified either as iodine pixels or bone pixels depending on their CT values [12]. However, in patients with severe stenosis, the contrast enhancement (CT value increase) may be weak in the lumen at the position of maximum stenosis because of the small number of iodine pixels. Also, partial volume effects may lead to an overestimation of plaque pixels resulting in an overestimation of severe stenosis. One solution may be to increase the injection rate of the contrast bolus to obtain higher CT values in the cross sections of maximum stenosis.

DE hard plaque removal offers the advantage that images from one single CT acquisition (albeit with a dual source) can be used for removing hard plaque and estimating calcified carotid stenosis. The unenhanced CT acquisition usually needed for BSCTA as a mask for subtraction thus becomes unnecessary, which reduces radiation dose to the patient and eliminates misregistration due to neck movement or arterial pulsation. The radiation dose of a dual-energy scan is comparable with a normal single-source scan. In fact, the average $CTDI_{vol}$ of our initial five carotid dual-source CTA studies was 11.1 mGy, while that of normal CTA with single-source scan was approximately 10.6 mGy, at 120 kV, 300 mA s (effective).

Conclusion

With DE hard plaque removal CTA, calcified plaques could be removed from carotid CTA images and high quality DSA-like imaging could be achieved. DE hard plaque removal is therefore useful for the evaluation of carotid stenosis with severe calcification.

References

1. North American Symptomatic Carotid Endarterectomy Trial Collaborators (1991) Beneficial effect of carotid endarterectomy in symptomatic patients with high-grade carotid stenosis. N Engl J Med 325:445–453
2. European Carotid Surgery Trialists' Collaborative Group (1991) MRC European Carotid Surgery Trial: interim results for symptomatic patients with severe (70–99%) or with mild (0–29%) carotid stenosis. Lancet 337:1235–1243
3. Barnett HJ, Taylor DW, Eliasziw M et al (1998) Benefit of carotid endarterectomy in patients with symptomatic moderate or severe stenosis. North American Symptomatic Carotid Endarterectomy Trial Collaborators. N Engl J Med 339:1415–1425
4. Anderson GB, Ashforth R, Steinke DE, Ferdinandy R, Findlay JM (2000) CT angiography for the detection and characterization of carotid artery bifurcation disease. Stroke 31:2168–2174
5. Moll R, Dinkel HP (2001) Value of the CT angiography in the diagnosis of common carotid artery bifurcation disease: CT angiography versus digital subtraction angiography and color flow Doppler. Eur J Radiol 39:155–162
6. Randoux B, Marro B, Koskas F et al (2001) Carotid artery stenosis: prospective comparison of CT, three-dimensional gadolinium-enhanced MR, and conventional angiography. Radiology 220:179–185
7. Josephson SA, Bryant SO, Mak HK, Johnston SC, Dillon WP, Smith WS (2004) Evaluation of carotid stenosis using CT angiography in the initial evaluation of stroke and TIA. Neurology 63:457–460
8. Lell M, Fellner C, Baum U et al (2007) Evaluation of carotid artery stenosis with multisection CT and MR imaging: influence of imaging modality and postprocessing. AJNR Am J Neuroradiol 28:104–110
9. Silvennoinen HM, Ikonen S, Soinne L, Railo M, Valanne L (2007) CT angiographic analysis of carotid artery stenosis: comparison of manual assessment, semiautomatic vessel analysis, and digital subtraction angiography. AJNR Am J Neuroradiol 28:97–103
10. Saba L, Sanfilippo R, Pirisi R, Pascalis L, Montisci R, Mallarini G (2007) Multidetector-row CT angiography in the study of atherosclerotic carotid arteries. Neuroradiology 49:623–637
11. Johnson TR, Krauss B, Sedlmair M et al (2007) Material differentiation by dual energy CT: initial experience. Eur Radiol 17:1510–1517
12. Flohr TG, McCollough CH, Bruder H et al (2006) First performance evaluation of a dual-source CT (DSCT) system. Eur Radiol 16:256–268
13. Venema HW, Hulsmans FJ, den Heeten GJ (2001) CT angiography of the circle of Willis and intracranial internal carotid arteries: maximum intensity projection with matched mask bone elimination-feasibility study. Radiology 218:893–898
14. Tomandl BF, Hammen T, Klotz E, Ditt H, Stemper B, Lell M (2006) Bone-subtraction CT angiography for the evaluation of intracranial aneurysms. AJNR Am J Neuroradiol 27:55–59
15. Lell MM, Ditt H, Panknin C et al (2007) Bone-subtraction CT angiography: evaluation of two different fully automated image-registration procedures for interscan motion compensation. AJNR Am J Neuroradiol 28:1362–1368
16. Silvennoinen HM, Ikonen S, Soinne L, Railo M, Valanne L (2007) CT angiographic analysis of carotid artery stenosis: comparison of manual assessment, semiautomatic vessel analysis, and digital subtraction angiography. AJNR Am J Neuroradiol 28:97–103

Ann Nucl Med (2008) 22:549–556
DOI 10.1007/s12149-008-0170-z

ORIGINAL ARTICLE

Three-dimensional SPECT reconstruction with transmission-dependent scatter correction

Antti Sohlberg · Hiroshi Watabe · Hidehiro Iida

Received: 26 March 2007 / Accepted: 8 January 2008

Abstract
Objective The quality of single-photon emission computed tomography (SPECT) imaging is hampered by attenuation, collimator blurring, and scatter. Correction for all of these three factors is required for accurate reconstruction, but unfortunately, reconstruction-based compensation often leads to clinically unacceptable long reconstruction times. Especially, efficient scatter correction has proved to be difficult to achieve. The objective of this article was to extend the well-known transmission-dependent convolution subtraction (TDCS) scatter-correction approach into a rapid reconstruction-based scatter-compensation method and to include it into a fast 3D reconstruction algorithm with attenuation and collimator-blurring corrections.
Methods Ordered subsets expectation maximization algorithm with attenuation, collimator blurring, and accelerated transmission-dependent scatter compensation were implemented. The new reconstruction method was compared with TDCS-based scatter correction and with one other transmission-dependent scatter-correction method using Monte Carlo simulated projection data of ^{99m}Tc-ECD and ^{123}I-FP-CIT brain studies.
Results The new reconstruction-based scatter compensation outperformed the other two scatter-correction methods in terms of quantitative accuracy and contrast measured with normalized mean-squared error, gray-to-white matter and striatum-to-background ratios, and also in visual quality. Highest accuracy was achieved when all the corrections (i.e., attenuation, collimator blurring, and scatter) were applied.
Conclusions The developed 3D reconstruction algorithm with transmission-dependent scatter compensation is a promising alternative to accurate and efficient SPECT reconstruction.

A. Sohlberg · H. Watabe · H. Iida (✉)
National Cardiovascular Center Research Institute,
5-7-1 Fujishiro-dai, Suita, Osaka 565-8565, Japan
e-mail: iida@ri.ncvc.go.jp

Keywords Statistical reconstruction · Scatter correction · Collimator-blurring correction · Attenuation correction

Introduction

The qualitative and quantitative accuracy of single-photon emission computed tomography (SPECT) is hampered by attenuation, collimator blurring, and scatter. Whereas attenuation and collimator blurring can nowadays be corrected in clinically acceptable times, accurate and efficient scatter correction has been proved to be a more difficult problem even though scatter compensation has received a lot of attention over the past two decades.

Scatter-correction methods can generally be divided into two groups: projection- and reconstruction-based methods. In the projection-based methods, scatter correction is usually performed by subtracting the scatter contribution from the projection data before the actual reconstruction [1]. These methods differ in how the scatter contribution is determined. The projection-based methods are usually easy to implement and fast to execute, but the overall improvement in image quality achieved with the scatter compensation, is often reduced by the noise increase in the reconstructed images owing to the subtraction procedure. The reconstruction-based scatter-correction methods, on the other hand, include the effects of scatter into the forward- and backprojec-

tors of the reconstruction algorithm without direct scatter subtraction. The reconstruction-based methods have been shown to achieve greater accuracy and lower noise level than the projection-based methods [2, 3], but they are often unsuitable for clinical practice owing to unacceptably long execution times because scatter calculations have to be repeated at each iteration of the reconstruction algorithm.

One promising projection-based scatter-correction method that has received a lot of attention is the transmission-dependent convolution subtraction (TDCS) algorithm [4]. TDCS has been used by our group to correct scatter in cerebral blood flow [5] and dopamine transporter [6] quantitation studies. Despite the relatively good performance of TDCS in the aforementioned experiments, TDCS is still hampered by the fact that as a projection-based scatter-correction method it relies on scatter subtraction, and also by the fact that it needs geometric mean (GM) projection data, which for example renders accurate collimator-blurring correction impossible.

Even though the traditional TDCS scatter correction has its limitations, the transmission-dependent scatter-modeling approach, when included in reconstruction-based scatter-compensation method, might prove to be useful. Hutton et al. [7, 8] used transmission-dependent scatter modeling to generate scatter projections, which could be included in iterative reconstruction algorithm to perform reconstruction-based scatter compensation in their two-step reconstruction procedure. In this method, Hutton first reconstructed a "scatter-free" image using broad-beam attenuation map. This image was then used as an input for a transmission-dependent scatter-modeling algorithm to calculate scatter projections, which were finally used as a constant additive term in the final "scatter-corrected" reconstruction according to the method of Bowsher and Floyd [9]. The objective of our work was to extend the two-step transmission-dependent scatter correction by Hutton to a "more natural" single-step scatter-compensation method and to include it into a fast 3D reconstruction algorithm with attenuation and collimator-blurring corrections. We also compared our new reconstruction method with Hutton's method and also with conventional TDCS scatter-correction approach in terms of quantitative accuracy, contrast, and image quality.

Materials and methods

Implementation of the reconstruction algorithms

The attenuation, collimator blurring, and scatter correction were implemented into ordered subsets expectation maximization (OSEM) algorithm [10]. The OSEM is given by

$$f_j^{\text{new}} = \frac{f_j^{\text{old}}}{\sum_{i\in S_n} a_{ij}} \sum_{i\in S_n} a_{ij} \frac{p_i}{\sum_k a_{ik} f_k^{\text{old}}}, \quad (1)$$

where f is the reconstructed image, p the measured projections, j (or k) reconstruction voxel index, i projection pixel index, a_{ij} the probability that emission from voxel j is detected in pixel i, and S_n the nth subset. The image update in OSEM consists of sequential forward- and backprojection operations. The estimated projections are obtained by forwardprojecting the current image estimate ($\sum_k a_{ik} f_k^{\text{old}}$) and correction terms that are used to update the old image are formed by backprojecting the ratio of the measured and estimated projections ($\sum_{i\in S_n} a_{ij} \frac{p_i}{\sum_k a_{ik} f_k^{\text{old}}}$).

Here, the forward- and backprojectors were implemented as rotation based [11] (Fig. 1a), which makes attenuation, collimator blurring, and scatter correction relatively straightforward to perform. Attenuation correction factors for each voxel were calculated simply by summing the rotated attenuation map along columns. Collimator blurring, on the other hand, was modeled by convolving each plane of the reconstruction matrix parallel to the projection plane with a collimator response kernel, which was spatially invariant in that plane (Fig. 1b) [12]. The collimator response function was assumed to be a 2D Gaussian function, whose full width at half maximum (FWHM) is linearly dependent on the distance (d_{col}) from the plane to the collimator

$$\text{FWHM}(d_{\text{col}}) = \alpha + \beta d_{\text{col}}. \quad (2)$$

Scatter modeling was implemented by slightly modifying the method presented by Hutton et al. [7, 8]. Hutton's method applies the rotating projectors and it compensates scatter as follows:

1. At each projection angle a "scatter-free" image, which has been obtained with reconstruction of the measured projection data using broad-beam attenuation coefficients, is first multiplied with monoexponential scatter kernel ($e^{-\alpha(d_{\text{tis}})r}$), whose slope ($\alpha$) is dependent on depth (d_{tis}) in tissue. A single scatter kernel is used for each plane at different tissue depth (see Fig. 1b).
2. Each point on each plane is then scaled with a transmission-dependent scatter-to-primary scatter fraction $SF_{S/P}$:

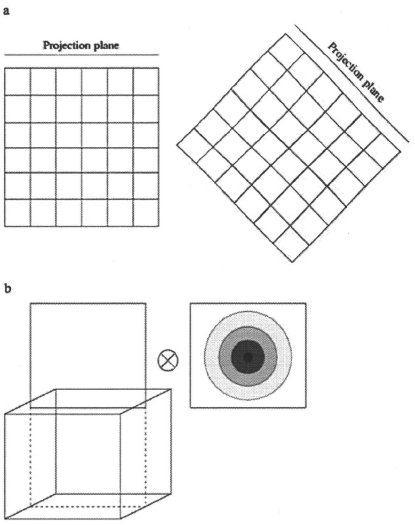

Fig. 1 **a** At each projection angle (two projection angles are shown), the rotating projector rotates the reconstruction matrix (single transverse plane is shown) so that its front face is aligned with the projection plane. The projections can be calculated simply by summing along columns of the reconstruction matrix. **b** Collimator response and scatter response modeling are realized by convolving each plane of the rotated reconstruction matrix (3D view is shown) parallel to the projection plane with an appropriate kernel

$$\mathrm{SF}_{\mathrm{S/P}} = A - B\left[\mathrm{e}^{-\sum_{k=j}^{\mathrm{skin}}\mu_k\Delta}\right]^{\gamma} - 1, \tag{3}$$

where A, B, and γ are the coefficients obtained from measurement [4], μ_k is the linear attenuation coefficient for voxel k and Δ voxel size.

3. The convolved and scaled voxel values are finally forwardprojected for obtaining scatter projection for the current projection angle.
4. After all the scatter projections are available, a new reconstruction is started. In this final reconstruction, the scatter projections obtained in the previous step are held as a constant term (s), which is added to the calculated projections $\left(\sum_k a_{ik} f_k^{\mathrm{old}} + s\right)$.

Our new method differs from Hutton's method by the fact that it does not use a pre-reconstructed broad-beam attenuation coefficient image to calculate the scatter projections, but instead we perform the convolution and scatter-fraction scaling using the current image estimate (f_j^{old}). Therefore, our scatter compensation can be presented as

1. In the forwardprojection step of the OSEM algorithm at each projection angle the current image estimate (f_j^{old}) is convolved with the scatter kernels.
2. Each point on each plane is then scaled with the transmission-dependent scatter fraction.
3. The convolved and scaled voxel values are finally forwardprojected and added to the forwardprojected primary counts.

We believe that our approach leads to more natural scatter compensation, reduces user intervention and execution time.

Scatter modeling makes reconstruction time consuming and therefore we used coarse-grid modeling [13] to provide further improvement in speed. In coarse-grid scatter modeling, scatter compensation is performed using larger voxel size than the actual reconstruction voxel size (in our case scatter was calculated using a 64 × 64 × 64 matrix in the case of a 128 × 128 × 128 reconstruction matrix). It is also worth pointing out that our method models scatter only in the forwardprojection step and do not use collimator-blurring compensation in scatter estimation.

The conventional TDCS was implemented according to Meikle et al. [4] using a single exponential convolution kernel and scatter-to-total scatter fractions ($\mathrm{SF}_{\mathrm{S/T}}$)

$$\mathrm{SF}_{\mathrm{S/T}} = \frac{1}{A - Bt_i^{\beta/2}}, \tag{4}$$

where t_i is transmission factor for projection pixel i. Convolution with the depth-independent scatter kernel ($\mathrm{e}^{-\alpha r}$) was performed to the measured projections (p_{meas}) after taking the GM and the result was scaled with the scatter fraction. The resulting scatter projections were subtracted from the measured projections for obtaining "scatter-free" projections (p_{nosc}):

$$p_{\mathrm{nosc}} = p_{\mathrm{meas}} - \mathrm{SF}_{\mathrm{S/T}}(p_{\mathrm{meas}} \otimes e^{-\alpha r}). \tag{5}$$

The scatter-free projections were finally reconstructed using OSEM.

Reconstruction al gorithm calibration

The parameters needed for collimator blurring and scatter correction were obtained from Monte Carlo simulations with the SIMIND simulator [14]. A low-energy

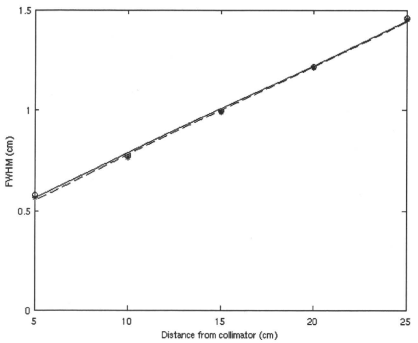

Fig. 2 Full width at half maximum as a function of distance from the collimator for ^{99m}Tc and ^{123}I. ^{99m}Tc measurements are shown with *circles* and the linear model fit (Eq. 2) as *solid line*, whereas ^{123}I measurements are presented with *stars* and the linear model fit as *dashed line*. The parameters α and β in Eq. 2 for ^{99m}Tc were 0.35 and 0.04 and for ^{125}I 0.33 and 0.04, respectively

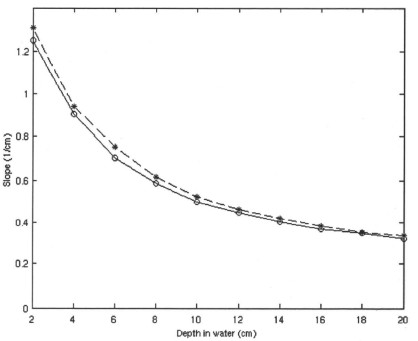

Fig. 3 Scatter kernel slope as a function of depth in water for ^{99m}Tc and ^{123}I. ^{99m}Tc measurements are shown with *solid line* with *circles* and ^{123}I measurements using *dashed line* with *stars*

high-resolution parallel hole collimator with 0.14 cm in hole diameter, a hole length of 2.7 cm, and a septal thickness of 0.018 cm was used. The pixel size in the simulations was set to 0.2 cm, and the projection data were acquired into a 128 × 128 matrix. Two sets of simulations were performed using ^{99m}Tc and ^{123}I as radionuclides. Symmetrical 15% energy window was centered on the photo-peak. For ^{123}I high-energy photons were not included in the simulations.

The FWHM as a function of distance was obtained by simulating point sources in air at different distances (5 cm, 10 cm, 15 cm, 20 cm, and 25 cm) from the collimator. FWHM was calculated by fitting a Gaussian function to a profile drawn through the center of the image, and the intercept (α) and slope (β) in Eq. 2 were obtained by fitting the linear model to the measurements (see Fig. 2).

The scatter kernel slope [$\alpha(d_{ds})$] for the reconstruction-based scatter-correction methods (Hutton's method and new method) was obtained by simulating a line source behind slabs of different thickness (2 cm, 4 cm, 6 cm, 8 cm, 10 cm, 12 cm, 14 cm, 16 cm, 18 cm, and 20 cm) of water. Low noise level planar images of the line sources were acquired and the slopes were calculated by fitting exponential functions to the scatter tails of profiles drawn through the center of the image. The results of this experiment are presented in Fig. 3. The slope for each plane at different depths in tissue in the reconstruction-based scatter correction was obtained by linear interpolation from the measurements. The slope for depth-independent scatter kernel in the conventional TDCS was set to 0.45 l/cm for ^{99m}Tc and 0.47 l/cm for ^{123}I.

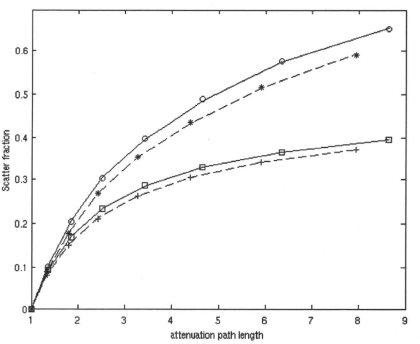

Fig. 4 Scatter fractions as a function of attenuation path length for ^{99m}Tc and ^{123}I. Scatter-to-primary ^{99m}Tc measurements are shown with *circles*, scatter-to-primary ^{123}I measurements with *stars*, scatter-to-total ^{99m}Tc measurements with *squares*, and scatter-to-total ^{123}I measurements are presented with plusses. The build-up equation fit (Eqs. 3, 4) for ^{99m}Tc is shown with *solid line* and for ^{123}I as *dashed line*. The build-up equation parameters *A*, *B*, and γ were 3.6, 2.6, and 0.13 for ^{99m}Tc and 4.3, 3.3, and 0.09 for ^{123}I. The same *A*, *B*, and γ parameters fitted well in both Eqs. 3 and 4

The *A*, *B*, and γ scatter-fraction coefficients were calculated by simulating point sources behind slabs of different thicknesses (2 cm, 4 cm, 6 cm, 8 cm, 10 cm, 12 cm, and 14 cm) of water. The scatter fractions were obtained from SIMIND, and these measurements were

fitted to Eqs. 3 and 4. Results from this experiment are presented in Fig. 4.

Brain phantom simulations

The new reconstruction-based scatter-correction method was compared with that of Hutton's method and to TDCS using the Zubal brain phantom [15]. The phantom was modified to represent the uptake of ^{99m}Tc-ECD (gray-to-white matter ratio 2.5:1) and ^{123}I-FP-CIT (striatum-to-background ratio 4:1). SIMIND was used to create low noise projection data of the phantoms, 120 angles over 360° circular orbit, by simulating approximately 70 MCts/projection using the same parameters as was used in determining the parameters for the reconstruction algorithms with the exception that pixel size was now 0.225 cm. Attenuation map was created by assigning correct densities for brain tissue and skull. The low-noise projections were then used to create noisy projection sets containing a total of 5 MCts for the ^{99m}Tc-ECD and 2 MCts for the ^{123}I-FP-CIT, which represent the average total count levels of ^{99m}Tc-ECD and ^{123}I-FP-CIT in clinical studies (personal communication Prof. Jyrki T. Kuikka, Kuopio University Hospital, Finland).

The noisy projection data were reconstructed using the new algorithm with (4 iterations and 15 subsets) and without collimator modeling (2 iterations and 15 subsets) and the GM projections with/without TDCS (2 iterations and 10 subsets). Reconstructions with collimator modeling used more iterations because of their slower convergence. Both reconstructions according to Hutton's method were performed with 2 iterations and 15 subsets. All the reconstructed images were post-filtered using a 3D Butterworth filter (cut-off 1.0 cycles/cm, order 5) according to clinical practice. The accuracy of the reconstruction methods was studied by comparing the overall accuracy of the reconstruction and correction methods and by calculating the normalized mean-squared error (NMSE) with respect to the known true counts (f_j^{true}):

$$\text{NMSE} = \frac{\sum_j \left(f_j^{\text{true}} - f_j\right)^2}{\sum_j f_j^{\text{true}^2}} \tag{6}$$

and the average gray-to-white matter and striatum-to-background ratios.

Results

Results of the Zubal brain phantom experiments are shown in Table 1. As can be seen, the reconstruction-based scatter-correction methods outperform the conventional TDCS in terms of contrast (gray-to-white matter and striatum-to-background ratios) and quantitative accuracy (normalized mean-squared errors). The new method is more accurate than that of Hutton's one, but the difference between the two is small. Highest accuracy is achieved when collimator-blurring correction is also applied during reconstruction. Indeed, collimator-blurring compensation might prove to be very useful in quantitative brain studies because it clearly reduces the partial volume effect offering higher accuracy. Interestingly, reconstructions from GM projections with only attenuation correction perform worse than reconstructions from normal projections. This is primarily caused by differences in attenuation correction. GM projections require projection space attenuation correction, whereas more accurate reconstruction space attenuation correction can be performed with normal projections. Examples of images with different reconstruction methods are shown in Figs. 5 and 6. The reconstruction-based scatter-compensation methods provide slightly better image quality than TDCS and the best result is obtained when collimator-blurring correction is also applied.

Table 1 Normalized mean-squared error (NMSE), gray-to-white matter ratio (GM:WM), and striatum-to-background ratio (STR:BG) for the ^{99m}Tc-ECD and ^{123}I-FP-CIT simulation studies

Corrections	NMSE_{ECD}	GM:WM	$\text{NMSE}_{\text{FP-CIT}}$	STR:BG
Attenuation[a]	0.186/0.182	1.11/1.17	0.136/0.134	2.19/2.24
Attenuation + $\text{scatter}_{\text{TDCS}}$	0.179	1.15	0.134	2.27
Attenuation + $\text{scatter}_{\text{Hutton}}$	0.173	1.24	0.127	2.29
Attenuation + $\text{scatter}_{\text{New}}$	0.172	1.25	0.126	2.29
Attenuation + $\text{scatter}_{\text{New}}$ + CDR	0.165	1.41	0.121	2.48

Results are presented for ordered subsets expectation maximization (OSEM) reconstruction with only attenuation correction, with attenuation and scatter correction [transmission-dependent convolution subtraction (TDCS)-based, Hutton's method and new method] and with attenuation, new scatter, and collimator-blurring correction (CDR). The attenuation correction only results are presented for two algorithms: geometric mean (GM) projection OSEM reconstruction, which has to be used for TDCS-based scatter correction and normal OSEM reconstruction which is used for Hutton's and new scatter-compensation methods

[a] The first values shown are the results of GM projection reconstruction and the second the results of normal reconstruction

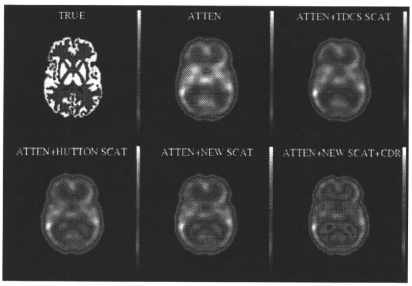

Fig. 5 Representative slices of the ^{99m}Tc-ECD study obtained with ordered subsets expectation maximization (OSEM) using only attenuation correction (reconstruction with normal projections), attenuation + transmission-dependent convolution subtraction (TDCS)-based scatter correction, attenuation + Hutton's scatter correction, attenuation + new scatter correction, and attenuation + new scatter + collimator-blurring (CDR) correction

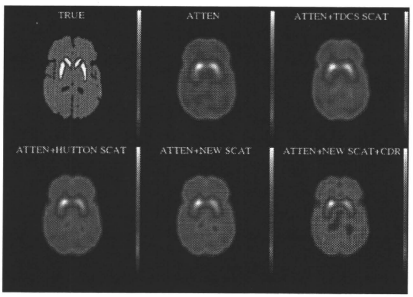

Fig. 6 Representative slices of the ^{123}I-FP-CIT study obtained with OSEM using only attenuation correction (reconstruction with normal projections), attenuation + TDCS-based scatter correction, attenuation + Hutton's scatter correction, attenuation + new scatter correction, and attenuation + new scatter + CDR correction

The average reconstruction times of the ^{99m}Tc-ECD and ^{123}I-FP-CIT Zubal phantom experiments are listed in Table 2. The TDCS is much faster than other methods, but it is worth noting that because of the GM projections TDCS uses only 60 projections in reconstruction, whereas the new method uses 120 projection images. TDCS also applies projection-based attenuation modeling as explained earlier, and therefore it does not require rotation of the attenuation map during the reconstruction, which saves time. Hutton's method is by far the slowest one because it requires pre-reconstruction to calculate scatter projections, but when the scatter projections are ready the actual scatter correction in the final reconstruction is faster than scatter compensation with the new method.

Table 2 Average reconstruction times for the ^{99m}Tc-ECD and ^{123}I-FP-CIT studies

Corrections	Time per iteration (s)
Attenuation[a]	67/212
Attenuation + $\text{scatter}_{\text{TDCS}}$	67
Attenuation + $\text{scatter}_{\text{Hutton}}$[b]	560 + 212
Attenuation + $\text{scatter}_{\text{New}}$	254
Attenuation + $\text{scatter}_{\text{New}}$ + CDR	336

Results are presented for OSEM reconstruction with only attenuation correction, with attenuation and scatter correction (TDCS-based, Hutton's method and new method) and with attenuation, new scatter, and collimator-blurring correction (CDR). The attenuation correction only results are presented for two algorithms: geometric mean (GM) projection OSEM reconstruction, which has to be used for TDCS-based scatter correction and normal OSEM reconstruction which is used for Hutton's and new scatter-compensation method. Calculation times have been obtained using 1.7 GHz Pentium processor with 1 GB RAM

[a] The first value shown is the time for GM projection reconstruction and the second is for normal reconstruction

[b] Pre-reconstruction and scatter forwardprojection calculation time + time for single iteration for the final reconstruction

Discussion

Here, we implemented a 3D reconstruction algorithm with transmission-dependent scatter modeling for efficient reconstruction-based scatter correction and compared it with reconstruction-based scatter-compensation method presented by Hutton et al. [7, 8], and with the conventional TDCS-based scatter-correction method [4]. The new algorithm proved to provide the highest accuracy according to Monte Carlo simulation studies of Zubal brain phantom (see Table 1). The new algorithm is also very advantageous because it allows easy incorporation of accurate attenuation and collimator-blurring corrections, which might prove to be very useful in high-quality SPECT imaging.

The presented scatter-correction method is relatively easy to implement and use. It requires two measurements for calibration: line source measurement to determine the scatter kernel slopes and point source measurement to determine the scatter fractions. These measurements need to be performed once for each radionuclide and collimator pair. In fact for lower-energy isotopes such as ^{99m}Tc, the scatter fractions have shown to be collimator independent [16] and therefore a single measurement might be sufficient for scatter-correction calibration for a large family of different collimators.

In addition to the ease of implementation, the execution time is of importance if a reconstruction method is to be used in clinical practice. Table 2 lists the calculation times per iteration for the scatter-correction methods. The TDCS-based scatter correction is clearly the fastest method, but the new method does not provide an extensive increase in computation time when compared with reconstruction without scatter correction. It is worth pointing out that even though the new method was accelerated using the coarse-grid scatter modeling, the reconstruction algorithm itself is not yet fully optimized. We believe that by further optimizing the structure of our reconstruction code and by replacing the current bilinear interpolation-based reconstruction grid rotation with a faster three-pass shear [17] method, we can still greatly reduce the computation time from the current 336 s/iteration.

This study has some limitations. First, testing and comparison of algorithms was performed using simplified simulated data. Simulated data were chosen, because they allowed easy comparison with true activity distributions, which are beneficial to finding small errors in initial reconstruction experiments. Simulations were performed as Monte Carlo simulations, which are known to have relatively good correspondence with real clinical data and we also tried to closely mimic clinical-imaging situations using appropriate noise levels and post-filters. On the other hand, it should be realized that even Monte Carlo simulations will probably produce results that are too good owing to the absence of errors in energy window calibration, non-uniformities, and so on that often hamper the quality of clinical data. Moreover, the high-energy photons of ^{123}I, which can penetrate or scatter at the collimator, were not included in the simulations, and the reconstructions were performed with noise-free and perfectly aligned attenuation maps. Both of these conditions are unnatural and their effects have to be investigated in detail in further studies.

Second, the metrics (NMSE and activity ratios) that were used to analyze the reconstructed images are simplistic, and more clinically relevant measures such as cerebral blood flow, binding potential, or task-based measures such as lesion detection are required in future studies to evaluate the true benefits of the presented reconstruction and corrections methods. Comparison of the new transmission-dependent scatter correction with other reconstruction-based scatter-correction methods such as in Beekman et al. [18] and Frey et al. [19] would also make an interesting topic for a further investigation.

In summary, we have proposed a 3D reconstruction algorithm with attenuation, collimator blurring, and transmission-dependent scatter correction, which shows promise as an efficient and accurate reconstruction method; however, further testing is still required to evaluate its true applicability in the clinical setting.

Acknowledgment This work was supported by grants from the Japan Society for the Promotion of Science.

References

1. Buvat I, Rodriguez-Villafuerte M, Todd-Pokropek A, Benali H, Di Paola R. Comparative assessment of nine scatter correction methods based on spectral analysis using Monte Carlo simulations. J Nucl Med 1995;36:1476–88.
2. Frey EC, Tsui BMW, Ljungberg M. A comparison of scatter compensation methods in SPECT: subtraction-based techniques versus iterative reconstruction with accurate modeling of the scatter response. Conference Record of the 1992 Nuclear Science Symposium and Medical Imaging Conference 1992;2: 1035–7.
3. Beekman FJ, Kamphuis C, Frey EC. Scatter compensation methods in 3D iterative reconstruction: a simulation study. Phys Med Biol 1997;42:1619–32.
4. Meikle SR, Hutton BF, Bailey DL. A transmission-dependent method for scatter correction in SPECT. J Nucl Med 1994; 35:360–7.
5. Iida H, Narita Y, Kado H, Kashikura A, Sugawara S, Shoji Y, et al. Effects of scatter and attenuation correction on quantitative assessment of regional cerebral blood flow with SPECT. J Nucl Med 1998;39:181–9.
6. Kim KM, Varrone A, Watabe H, Shidahara M, Fujita M, Innis RB, et al. Contribution of scatter and attenuation compensation to SPECT images of nonuniformly distributed brain activities. J Nucl Med 2003;44:512–9.
7. Hutton BF, Osiecki A, Meikle SR. Transmission-based scatter correction of 180° myocardial single-photon emission tomographic studies. Eur J Nucl Med 1996;23:1300–8.
8. Hutton BF, Baccarne V. Efficient scatter modelling for incorporation in maximum likelihood reconstruction. Eur J Nucl Med 1998;25:1658–65.
9. Bowsher JE, Floyd CE. Treatment of Compton scattering in maximum-likelihood expectation maximization reconstructions of SPECT images. J Nucl Med 1991;32:1285–91.
10. Hudson HM, Larkin RS. Accelerated image reconstruction using ordered subsets of projection data. IEEE Trans Med Imaging 1994;13:601–9.
11. Zeng GL, Gullberg GT. Frequency domain implementation of the three-dimensional geometric point response correction in SPECT imaging. IEEE Trans Nucl Sci 1992;39:1444–53.
12. Zeng GL, Gullberg GT, Bai C, Christian PE, Trisjono F, Di Bella EVR, et al. Iterative reconstruction of fluorine-18 SPECT using geometric point response correction. J Nucl Med 1998; 39:124–30.
13. Kadrmas DJ, Frey EC, Karimi SS, Tsui BMW. Fast implementations of reconstruction-based scatter compensation in fully 3D SPECT image reconstruction. Phys Med Biol 1998;43: 857–73.
14. Ljungberg M, Strand SE. A Monte Carlo program for the simulation of scintillation camera characteristics. Comput Methods Programs Biomed 1989;29:257–72.
15. Zubal IG, Harrell CR, Smith EO, Rattner Z, Gindi G, Hoffer PB. Computerized three-dimensional segmented human anatomy. Med Phys 1994;21:299–302.

16. Kim KM, Watabe H, Shidahara M, Ishida Y, Iida H. SPECT collimator dependency of scatter and validation of transmission-dependent scatter compensation methodologies. IEEE Trans Nucl Sci 2001;48:689–96.
17. Di Bella EVR, Barclay AB, Eisner RL, Schafer RW. A comparison of rotation-based methods for iterative reconstruction algorithms. IEEE Trans Nucl Sci 1996;43:3370–6.
18. Beekman FJ, de Jong HW, van Geloven S. Efficient fully 3-D iterative SPECT reconstruction with Monte Carlo-based scatter compensation. IEEE Trans Med Imaging 2002;21: 867–77.
19. Frey EC, Ju ZW, Tsui BMW. A fast projector-backprojector pair modeling the asymmetric, spatially varying scatter response function for scatter compensation in SPECT imaging. IEEE Trans Nucl Sci 1993;40:1192–7.

Eur J Nucl Med Mol Imaging
DOI 10.1007/s00259-007-0654-4

ORIGINAL ARTICLE

Absolute quantitation of myocardial blood flow with ^{201}Tl and dynamic SPECT in canine: optimisation and validation of kinetic modelling

Hidehiro Iida · Stefan Eberl · Kyeong-Min Kim · Yoshikazu Tamura · Yukihiko Ono · Mayumi Nakazawa · Antti Sohlberg · Tsutomu Zeniya · Takuya Hayashi · Hiroshi Watabe

Received: 18 September 2007 / Accepted: 4 November 2007

Abstract
Purpose ^{201}Tl has been extensively used for myocardial perfusion and viability assessment. Unlike ^{99m}Tc-labelled agents, such as ^{99m}Tc-sestamibi and ^{99m}Tc-tetrofosmine, the regional concentration of ^{201}Tl varies with time. This study is intended to validate a kinetic modelling approach for in vivo quantitative estimation of regional myocardial blood flow (MBF) and volume of distribution of ^{201}Tl using dynamic SPECT.
Methods Dynamic SPECT was carried out on 20 normal canines after the intravenous administration of ^{201}Tl using a commercial SPECT system. Seven animals were studied at rest, nine during adenosine infusion, and four after beta-blocker administration. Quantitative images were reconstructed with a previously validated technique, employing OS-EM with attenuation-correction, and transmission-dependent convolution subtraction scatter correction. Measured regional time–activity curves in myocardial segments were fitted to two- and three-compartment models. Regional MBF was defined as the influx rate constant (K_1) with corrections for the partial volume effect, haematocrit and limited first-pass extraction fraction, and was compared with that determined from radio-labelled microspheres experiments.
Results Regional time–activity curves responded well to pharmacological stress. Quantitative MBF values were higher with adenosine and decreased after beta-blocker compared to a resting condition. MBFs obtained with SPECT (MBF_{SPECT}) correlated well with the MBF values obtained by the radio-labelled microspheres (MBF_{MS}) ($MBF_{SPECT}=-0.067+1.042\times MBF_{MS}$, $p<0.001$). The three-compartment model provided better fit than the two-compartment model, but the difference in MBF values between the two methods was small and could be accounted for with a simple linear regression.
Conclusion Absolute quantitation of regional MBF, for a wide physiological flow range, appears to be feasible using ^{201}Tl and dynamic SPECT.

Keywords Myocardial blood flow · Dynamic SPECT · Thallium-201 · Compartment model · Quantitation

H. Iida (✉) · S. Eberl · K.-M. Kim · M. Nakazawa · A. Sohlberg · T. Zeniya · T. Hayashi · H. Watabe
Department of Investigative Radiology,
National Cardiovascular Center Research Institute,
Fujishiro-dai,
Suita City, Osaka 565-8565, Japan
e-mail: iida@ri.ncvc.go.jp

S. Eberl
PET and Nuclear Medicine Department,
Royal Prince Alfred Hospital,
Missenden Road,
Camperdown, NSW 2050, Australia

Y. Tamura
Department of Cardiology, Akita Kumiai General Hospital,
1-1-1, Nishi-bukuro, Iijima,
Akita City 011-0948, Japan

Y. Ono
Akita Research Institute of Brain,
6-10, Senshu-Kubota Machi,
Akita City 010-0874, Japan

Introduction

Myocardial perfusion imaging using Thallium-201 (^{201}Tl) is well established in routine clinical practice for detecting